Newly Discovered z ∼ 5 Quasars Based on Deep Learning and Bayesian Information Criterion

Suhyun Shin[1], Myungshin Im[1], Yongjung Kim[2,3], and Linhua Jiang[3]

[1]SNU Astronomy Research Center, Astronomy Program, Dept. of Physics & Astronomy, Seoul National University,
1 Gwanak-ro, Gwanak-gu, Seoul 08826, Republic of Korea; suhyun.shin.s2@gmail.com, myungshin.im@gmail.com
[2]Department of Astronomy and Atmospheric Sciences, College of Natural Sciences, Kyungpook National University,
Daegu 41566, Republic of Korea
[3]Kavli Institute for Astronomy and Astrophysics, Peking University, Beijing 100871, People's Republic of China

Abstract: We report the discovery of four quasars with $M_{1450} \gtrsim -25.0$ mag at $z \sim 5$ and supermassive black hole mass measurement for one of the quasars. They were selected as promising high-redshift quasar candidates via deep learning and Bayesian information criterion, which are expected to be effective in discriminating quasars from the late-type stars and high-redshift galaxies. The candidates were observed by the Double Spectrograph on the Palomar 200-inch Hale Telescope. They show clear Lyα breaks at about 7000–8000 Å, indicating they are quasars at $4.7 < z < 5.6$. For HSC J233107-001014, we measure the mass of its supermassive black hole (SMBH) using its C IV $\lambda 1549$ emission line. The SMBH mass and Eddington ratio of the quasar are found to be $\sim 10^8$ $M_\odot$ and ~ 0.6, respectively. This suggests that this quasar possibly harbors a fast growing SMBH near the Eddington limit despite its faintness ($L_{\rm Bol} < 10^{46}$ erg s^{-1}). Our 100% quasar identification rate supports high efficiency of our deep learning and Bayesian information criterion selection method, which can be applied to future surveys to increase high-redshift quasar sample.

Key words: galaxies: active — galaxies: quasars: general — methods: data analysis — methods: observational — techniques: spectroscopic

1. Introduction

Quasars are one of the most powerful astrophysical sources in the universe with a bolometric luminosity, $L_{\rm Bol} \gtrsim 10^{45}$ erg s^{-1} (e.g., Hickox & Alexander 2018). Owing to their high luminosities, we can find them even in the distant universe ($z > 7$; Mortlock et al. 2011; Bañados et al. 2018; Matsuoka et al. 2019; Yang et al. 2020a; Wang et al. 2021). The discovery of quasars in the early universe enables us to investigate how the intergalactic medium (IGM) was ionized and supermassive black holes (SMBHs) grew (e.g., Fan et al. 2006; Trakhtenbrot et al. 2011; Kim et al. 2018; Onoue et al. 2019; Yang et al. 2020b). By constructing the quasar luminosity function (LF) at $z \gtrsim 4$ with several reasonable assumptions, the contribution of quasars to keep the ionized state of the IGM can be estimated (Jiang et al. 2016; Akiyama et al. 2018; Matsuoka et al. 2018; McGreer et al. 2018; Kim et al. 2020; Shin et al. 2020). Given the short time available for SMBHs to grow between the birth of seed BHs and the age of the universe where the highest redshift known quasars reside, examining the properties of the early universe quasars can give us insights on how the SMBH became to exist (e.g., Bañados et al. 2018; Yang et al. 2020a).

Although the expected contribution to the UV background at $z \sim 5$ of quasars with the rest-frame absolute magnitude at 1450 Å (M_{1450}) between -25 and -22 mags are comparable to or greater than that of brighter quasars (Kim et al. 2020), the number of the currently identified faint quasars with $-25 < M_{1450} < -22$ is much less than the number of brighter quasars so far. This is because previous quasar searches have mostly relied on wide-field surveys with shallow depths. The situation is improving with deeper data becoming available for high-redshift quasar search: the Canada–France–Hawaii Telescope Legacy Survey (CFHTLS; Gwyn 2012); the Dark Energy Survey (DES; Dark Energy Survey Collaboration et al. 2016); the Hyper Suprime-Cam Subaru Strategic Program (HSC-SSP; Aihara et al. 2019); the Infrared Medium-deep Survey (IMS; Im et al. 2022, in preparation).

However, finding faint quasars is more challenging than bright quasar search, even with deeper images. High-redshift quasars can be identified by the strong break in their spectral energy distributions (SEDs) caused by the redshifted Lyman break (Jiang et al. 2016; Jeon et al. 2017; McGreer et al. 2018; Kim et al. 2019; Shin et al. 2020). However, as we go fainter in magnitude, there is a rapid increase in the number of other types of objects, such as primarily late-type stars and high redshift galaxies, which mimic this break. Conventional color selection considering only a few broadband colors is not enough to reject lots of contaminant sources in faint quasar candidates (Matsuoka et al. 2018; Niida et al. 2020, hereafter, N20). SED model fitting is a physically meaningful approach

CORRESPONDING AUTHOR: M. Im

for searching quasars (Reed et al. 2017). However, it would require a considerable amount of computing resources if one hopes to find faint quasars among many contaminants.

In our previous work (Shin et al. 2022), we developed a novel method for selecting quasar candidates adopting the deep learning and the Bayesian information criterion (BIC). We applied this method to the HSC-SSP data that reaches a 5-σ depth of $i \sim 26$ mag for point source detection (Aihara et al. 2019) which corresponds to $M_{1450} \sim -20$ mag for $z \sim 5$ quasars. We identified 35 faint quasar candidates, five being previously known quasars.

In this paper, we report our spectroscopic observation of four quasar candidates with $i < 23$ mag as an attempt to further confirm the effectiveness of our new quasar selection method. In Section 2, we describe the photometric selection process for quasars at z $\sim$ 5 in brief. The specification for the spectroscopic observation is explained in Section 3. Section 4 includes the spectral fitting procedure and black hole (BH) mass measurement from C IV emission line. The efficiency of our quasar selection is addressed in Section 5. Section 6 summarizes our findings. We assume cosmological parameters $\Omega_M = 0.3$, $\Omega_\Lambda = 0.7$ and $H_0 = 70 \mathrm{~km \, s^{-1} \, Mpc^{-1}}$ throughout the paper. We adopted the AB magnitude system for representing a flux measured in each filter (Oke & Gunn 1983) and used the dust map of Schlegel et al. (1998) to correct fluxes for the Galactic extinction.

2. QUASAR SELECTION

Faint quasar candidates at $z \sim 5$ were selected in our previous work (Shin et al. 2022). Here, we briefly explain how the quasar candidates were selected.

2.1. Photometric Data

The HSC-SSP has Wide, Deep, and UltraDeep layers. Taking advantage of deep images ($i \sim 26$ mag) and moderate survey area ($27 \mathrm{~deg^2}$), we choose the Deep layer to search quasars among the layers. The Deep layer consists of four fields covered by five broadbands (g, r, i, z, y) and two narrow-bands ($NB816$, $NB921$). The 5-σ image depths of broadbands (g, r, i, z, y) are (27.3, 26.9, 26.7, 26.3, and 25.3). For $NB816$ and $NB921$, the depths are 26.1 and 25.9 mag, respectively.

We retrieved a source catalog of the second public data release (PDR2) of the HSC-SSP. To exclude objects with unreliable photometry, we adopted flags evaluating influences from the bad pixel, cosmic ray, saturation at the center of an object, abnormal background level, and the location of an object on an image. Also, we constrained that a source should be a primary object with detection in the i-band. After excluding the flagged objects, the resulting effective survey area of the Deep layer for our quasar search became $\sim 15.5 \mathrm{~deg^2}$ based on a random source catalog in HSC-SSP data archival system (Coupon et al. 2018), somewhat smaller than the nominal HSC-SSP Deep survey area of $27 \mathrm{~deg^2}$. The number of sources in the catalog
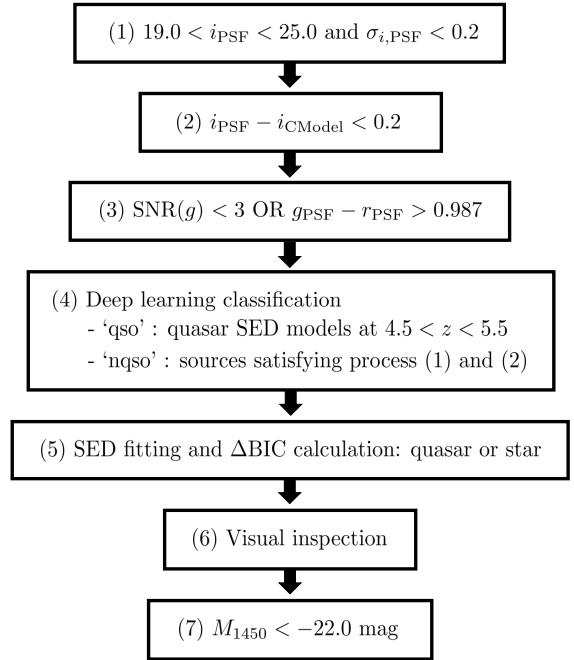

Figure 1. Flow chart for the entire quasar selection process.

is 3.5 million. In this study, we use two magnitude systems: the point-spread function (PSF) magnitude and the CModel magnitude (CModel).

2.2. SED Models

Due to the small sample size of spectroscopically confirmed quasars at $z \sim 5$ in the Deep layer of the HSC-SSP (<10), quasar SED models were used for training deep learning models and calculating BIC. Stellar SED models are also necessary to do SED fitting. Since these SED models were introduced in detail in Shin et al. 2022, here we explained them in brief.

Our quasar SED models have four free parameters: redshift (z_{SED}), continuum slope (α_λ), equivalent width of Lyα and N V λ1240 (EW), and M_{1450}. We created a composite SED by adopting the SED at $\lambda < 1450$ Å from Lusso et al. (2015) and the redder part from Selsing et al. (2016). Then, the Lyα+N V equivalent width and the continuum slopes are adjusted. The IGM attenuation model of Inoue et al. (2014) was adopted.

For the stellar SED models, we used the BT-Settl models (Allard et al. 2013) which have five free parameters: effective temperature (T_{eff}), surface gravity ($\log g$), metallicity ([M/H]), alpha-element enrichment ([α/M]), and a normalization factor (f_N).

2.3. Quasar Selection Process

We applied multiple criteria sequentially. Figure 1 shows the sequence of our selection.

First, we selected objects with $19 < i_{PSF} < 25$ and magnitude error < 0.2 mag (the process (1)). Then, we

Table 1
General information of the targets and spectroscopic observations

ra (J2000)	dec (J2000)	g [mag]	r [mag]	i [mag]	$NB816$ [mag]	z [mag]	$NB921$ [mag]	y [mag]	Date	Exp Time [sec]
02:17:33.44	−4:44:44.32	25.7	23.7	22.2	22.4	22.1	22.1	22.3	2020 Nov 19	1500
16:18:27.28	55:17:48.51	25.3	22.7	21.1	21.1	20.9	20.9	20.8	2021 Jul 13	600
23:27:13.22	0:05:47.92	>27.3	25.1	22.3	21.3	22.0	21.7	21.8	2020 Nov 19	1800
23:31:07.00	−0:10:14.52	>27.3	24.4	22.6	23.2	22.6	21.8	22.7	2020 Nov 19	1800

The magnitude errors are mostly less than 0.03 mag.

eliminated extended sources by applying the extendedness cut of $i_{PSF} - i_{CModel} < 0.2$ (the process (2)). With this procedure, we could include about 98.4 % of point sources identified by an I-band catalog of the Hubble Space Telescope (HST) Advanced Camera for Surveys (Leauthaud et al. 2007). The number of candidates satisfying the process (1) and (2) was 333,780. Among them, there are six spectroscopically confirmed quasars at $4.5 < z < 5.5$ (McGreer et al. 2013; Pâris et al. 2018; Shin et al. 2020).

Since faint quasars at $z \sim 5$ have the strong IGM absorption lines in the blueward of the Lyα emission line, they tend to show a weak signal to noise ratio (SNR < 3) in the g-band or large $g - r$ color. To focus on the quasars at $4.5 < z < 5.5$, we limited the $g - r$ color to 0.987, which is the minimum $g - r$ value for quasar models at the redshift range. The number of candidates was 125,644.

After choosing the red objects, we performed classification using deep learning. We trained 100 models to predict a class of an object based on its HSC-SSP photometry information. Our trained models assume that the red objects belong to one of two classes: quasars at $z \sim 5$ ('qso') or non-quasar sources ('nqso'). Training set for the 'qso' comprised of 100,000 randomly sampled quasar models at $4.5 < z < 5.5$. For training 'nqso' class, 100,000 randomly sampled point sources with $19 < i < 25$ and $\sigma_i < 0.2$ were used. Combining results of 100 deep learning models, we achieved an average accuracy larger than 99 % for the 'qso' class. 1,599 candidates were selected in our ensemble learning.

To compensate for the simple approximation used in the deep learning and deal with possible misclassified 'nqso' objects, we carried out SED fitting of 1,599 deep-learning-selected candidates using quasar and stellar SED models and compare the best-fit models by adopting the BIC. For each best-fit model, the BIC value can be calculated as,

$$\mathrm{BIC} = \chi^2 + k \times \ln n \,,$$

where k is the number of free parameters in the model, n is the number of the data, and χ^2 is the chi-square value for the model. The BIC imposes the penalty term to the model with a large k, so a fair comparison between given models becomes possible. The difference between the BIC values, ΔBIC, is defined as

$$\Delta\mathrm{BIC} = \mathrm{BIC}_{star} - \mathrm{BIC}_{quasar} \,.$$

The larger ΔBIC is, the more likely it is a quasar. We considered the minimum value of the ΔBIC as 10 (Liddle 2007). The number of the BIC-selected candidates was 78.

We visually inspected multi-band HSC-SSP images to remove candidates for which the photometry could be affected by satellite tracks, nearby bright stars, optical ghosts, and scattered lights. Among the 78 BIC-selected candidates, 53 candidates passed the visual inspection.

Finally, we restricted the M_{1450} of the candidate to be brighter than −22.0 mag where the number density of quasar candidates can dramatically increase due to the galaxy contamination (N20, Shin et al. 2022). The number of the final quasar candidates is 35. Five out of 35 candidates are known quasars at $z \sim 5$ (McGreer et al. 2013; Shin et al. 2020). Another four candidates were selected to be promising candidates selected in McGreer et al. (2018), Chaves-Montero et al. (2017) and Shin et al. (2020). Among these four candidates, a spectrum of one candidate (Shin et al. 2020) was obtained in this study.

3. SPECTROSCOPY

We conducted spectroscopic observations for four candidates with $i_{PSF} < 23$ mag between 2020 November and 2021 July. Note that one of the targets, IMS J161827+551748 was also selected using a different selection method that included medium-band data (Shin et al. 2020). We utilized the Double Spectrograph (DBSP) on the 200-inch Hale Telescope in the Palomar Observatory (PID: CTAP2020-B0043 and CTAP2021-A0032, PI: Y. Kim). Using the dichroic filter, the DBSP can observe the red and blue channels simultaneously. The dichroic filter we used was D55. We set a long-slit mode with a slit of which the width and length correspond to 1.5 and 128 arcseconds. The 316 (600) lines/mm grating with a wavelength of 7500 (4000) Å was chosen for the red (blue) channel. The exposure time was ∼1200 to 1800 seconds. The typical seeing during the observing period was ∼1.1 to 1.5 arcseconds.

After acquiring the spectroscopic data, we pre-processed the data with a python package, PypeIt (Prochaska et al. 2020a,b). Owing to the expected IGM absorption in the blue channel, we only considered the red channel in this study. The PypeIt can automatically subtract bias, perform flat-fielding, give a wave-

Table 2
Best-fit spectral parameters

id	$z_{\mathrm{Ly}\alpha}$	z_{spec}	α_λ	$\log(\mathrm{EW})$	M_{1450} [mag]
HSC J021733-044444	4.807	$4.783^{+0.003}_{-0.003}$	$-1.58^{+0.35}_{-0.37}$	$2.38^{+0.05}_{-0.05}$	$-23.88^{+0.06}_{-0.06}$
HSC J161827+551748	4.754	$4.726^{+0.005}_{-0.008}$	$-1.94^{+0.53}_{-0.56}$	$1.71^{+0.12}_{-0.17}$	$-25.13^{+0.06}_{-0.06}$
HSC J232713+000547	5.591	$5.561^{+0.003}_{-0.006}$	$-1.40^{+0.74}_{-0.70}$	$2.51^{+0.06}_{-0.06}$	$-24.44^{+0.10}_{-0.09}$
HSC J233107-001014	4.974	$4.950^{+0.002}_{-0.004}$	$-0.58^{+0.52}_{-0.56}$	$2.62^{+0.10}_{-0.10}$	$-23.03^{+0.19}_{-0.16}$

length solution, and model the sky background. To do wavelength calibration, we used a HeNeAr lamp. Since our targets are too faint to be detected with a default algorithm, we manually extracted the fluxes of a standard star and the targets. We adjusted the spatial and spectral locations of the extraction window and its size to maximize the signal-to-noise ratio of each spectrum.

After reducing the data, we calculated a sensitivity function by comparing the observed fluxes of a standard star, Feige110, with its actual fluxes. After the sensitivity correction, we rescaled the spectrum using HSC-SSP i-band magnitude to correct for a possible flux loss due to the finite size of the slit width.

From the full width at half maximum (FWHM) of sky emission lines, we estimated a spectral resolution, $R = 800$–1300, which varied depending on the observed wavelength and the observation date. Table 1 shows the coordinate, HSC-SSP photometry, observation date, and exposure time for the candidates.

4. RESULT

4.1. Spectral Fitting

To increase the SNR of each spectrum, the spectrum was binned at intervals of 6–9 Å (5–6 pixels), corresponding to FWHM from its R. Each flux in each bin was weighted by the inverse of its squared flux uncertainty. The weighted mean flux is to be a representative value of each bin. After binning, the SNRs of the spectra reach 5 to 15 at their emission lines, and 2 to 3 at their continua. Figure 2 shows the binned spectra of the four objects. All four objects show predominant and broad Lyα emission lines with sufficient SNR $\sim$ 10 and sharp breaks at the blueward of the line due to the IGM absorption, confirming their nature as high-redshift quasars.

To estimate the spectroscopic redshift (z_{spec}), we performed a spectrum fitting based on quasar SED models to the binned spectra (please refer to Section 2.2). The best-fit model was obtained by using Markov Chain Monte Carlo (MCMC) method (Foreman-Mackey et al. 2013). From the sampled posterior distribution of the parameter, we obtained the best-fit parameter and its error as the median and the 68% equal-tailed interval of the distribution (Table 2). Due to the low SNR of the continuum, the uncertainties of the parameters are somewhat large except for z_{spec}, implying the role of the clear Lyα emission line in constraining the z_{spec}. These quasars have $M_{1450} = -23.0$
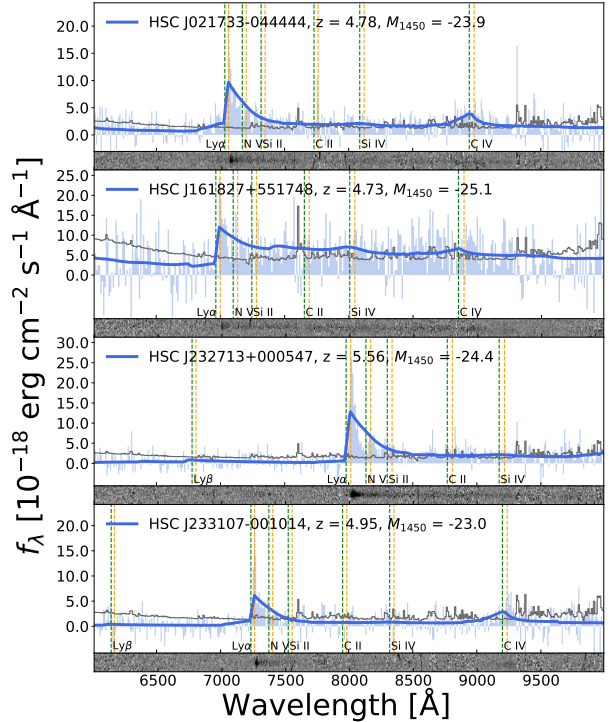

Figure 2. The 1-d and 2-d spectra of four observed quasar candidates in sequence. The skyblue bins and gray lines correspond to the 1-d binned spectra and their 1-σ flux errors, respectively. The blue thick lines are the best-fit quasar SED model. Several dominant lines in a typical quasar spectrum are marked as green (orange) vertical lines of which the locations depend on z_{spec} ($z_{\mathrm{Ly}\alpha}$). The 2-d spectra are shown in an inverted gray scale.

to -25.2 mag at $z_{\mathrm{spec}} = 4.7$ to 5.6.

In addition to the best-fit z_{spec}, we calculated the $z_{\mathrm{Ly}\alpha}$ by comparing the location of the strongest point in the Lyα emission line to the rest wavelength of the line (1216 Å). Although the blueward of the Lyα emission line was attenuated by the neutral hydrogen in the IGM, the $z_{\mathrm{Ly}\alpha}$ is still consistent with the locations of the strong emission lines such as Lyα and C IV, especially for HSC J233107-001014. The $z_{\mathrm{Ly}\alpha}$ values are also provided in Table 2.

4.2. BH Mass and Eddington Ratio

One interesting question is whether high-redshift quasars are more vigorously growing than lower-redshift
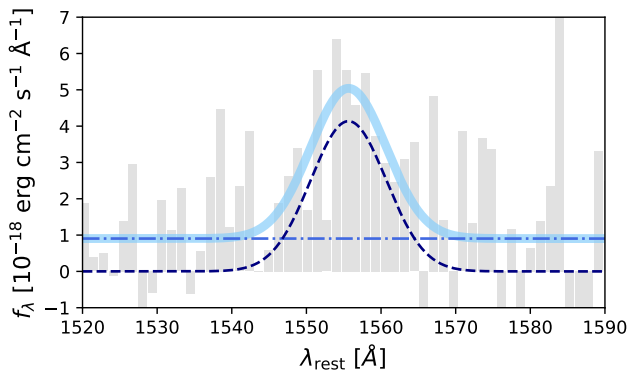
Figure 3. Spectral modeling for the C IV emission line. We plot the binned spectrum of HSC J233107-001014 in the gray bar. The thick line indicates the best-fit model which is the summation of the power-law continuum and C IV emission line modeled as a single Gaussian distribution. The former and latter is plotted in the dot-dashed line and the dashed line, respectively.
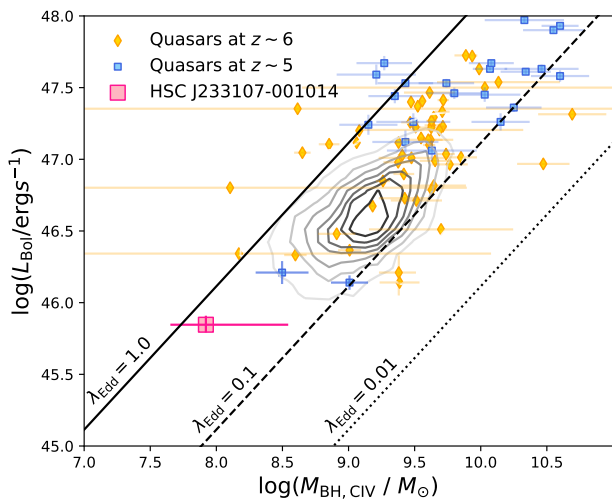

Figure 4. M_{BH}-L_{Bol} distributions of quasars, from M_{BH} measurements based on C IV emission line. The contours show the locations of the quasars at $z \sim 2$ on the M_{BH}-L_{Bol} plane (Shen et al. 2011). The blue squares represent quasars at $z \sim 5$ (Jun et al. 2015; Ikeda et al. 2017), while the gold diamonds indicate quasars at $z \sim 6$ (Jiang et al. 2007; Kim et al. 2018; Shen et al. 2019). Our faint quasar at $z \sim 5.0$ is marked with the pink square. The solid, dashed, and dotted lines in the panels are corresponds to $\lambda_{Edd} = 1, 0.1,$ and 0.01, respectively.

quasars (Willott et al. 2010; Kim et al. 2018; Onoue et al. 2019; Shen et al. 2019). Recent studies of quasars at $z \gtrsim 6$ have found that SMBHs in the bright quasars are vigorously growing with the Eddington ratios (λ_{Edd}) of $\lambda_{Edd} \sim 1$ (Mortlock et al. 2011; Bañados et al. 2018; Yang et al. 2020a). On the other hand, other studies find that fainter quasars at $z > 6$ have $\lambda_{Edd} \sim 0.1$, on par with quasars at $z = 2$ to 3 (Shen et al. 2011; Mazzucchelli et al. 2017; Kim et al. 2018; Onoue et al. 2019;

Shen et al. 2019). Here, we investigate the supermassive black hole mass (M_{BH}) and λ_{Edd} of one of our sample, HSC J233107-001014 for which C IV is detected.

First, we transferred the observed frame to rest frame by using z_{spec}. Then, we modeled continuum using a power-law function ($f_\lambda = \zeta \lambda^{\alpha_\lambda}$). Although the continuum consists of not only the power-law continuum but also Fe II complex and Balmer continuum, we considered the former only due to the lack of sensitivity in its overall spectrum and an insignificant influence of the Fe II emissions on the C IV line properties (e.g., Shen et al. 2011). We fitted the power-law continuum to the fluxes of which the wavelength range is not close to those of the broad emission lines (e.g., Lyα, C IV). To prevent large uncertainty of α_λ caused by poor SNR $\sim$ 1–3 of the binned spectrum, it was inevitable to use global parts of the spectrum corresponding to $\lambda = 1260$–1510 and 1580–1660, and assume $\zeta = 1$. The fitted power-law continuum was subtracted from the spectrum.

We also modeled the continuum-subtracted C IV emission line with a single Gaussian profile. Even though the C IV line is frequently regarded as the sum of multiple Gaussian profiles (e.g., Jun et al. 2015; Zuo et al. 2020), we did not include additional Gaussian components because the spectrum has a SNR too low to discern multiple components. To estimate the FWHM of the C IV emission line ($FWHM_{C IV}$) and its error, we generated 10,000 mock spectra by assuming the probability density function of the flux follows a Gaussian distribution. We calculated an $FWHM_{C IV, init}$ for each spectrum, then the FWHM of our instrument ($FWHM_{int} \sim 230$ km s^{-1}) was subtracted from the estimated FWHMs, resulting in $FWHM_{C IV} = \sqrt{FWHM_{C IV, init}^2 - FWHM_{int}^2}$. Adopting 16 and 84 percentiles of the $FWHM_{C IV}$ histogram as 1-σ uncertainties, the $FWHM_{C IV}$ is 2230^{+1560}_{-640} km s^{-1}. The spectral fitting result of the C IV line is shown in Figure 3.

The mass scaling relation based on the C IV line (Vestergaard & Peterson 2006) is expressed as,

$$M_{BH} = \left[\frac{FWHM_{C IV}}{1000 \text{ km s}^{-1}} \right]^2 \left[\frac{\lambda L_\lambda (1350 \text{ Å})}{10^{44} \text{ erg s}^{-1}} \right]^{0.53} \times 10^{6.6} \ M_\odot.$$

$L_\lambda(1350$ Å) is calculated from the best-fit SED model for the spectrum of HSC J233107-001014. The resulting $\log(M_{BH}/M_\odot)$ is $7.92^{+0.62}_{-0.27}$ for the virial factor of 5.1 (Woo et al. 2013).

We caution that C IV-based M_{BH} could be systematically biased than the Balmer line-based M_{BH}, since the C IV line profile could be seriously affected by non-virial motion (e.g., Sulentic et al. 2017). To correct for systematic bias, some studies have considered the relation between physical parameters (e.g., C IV blueshift, Eddington ratio, C IV line asymmetry, and so on) and the difference between C IV-based and Balmer-based BH masses (Coatman et al. 2017; Marziani et al. 2019; Zuo et al. 2020). Although the corrected $FWHM_{C IV}$ based on the relations could improve the M_{BH} estimates, we did not apply the correction due to large
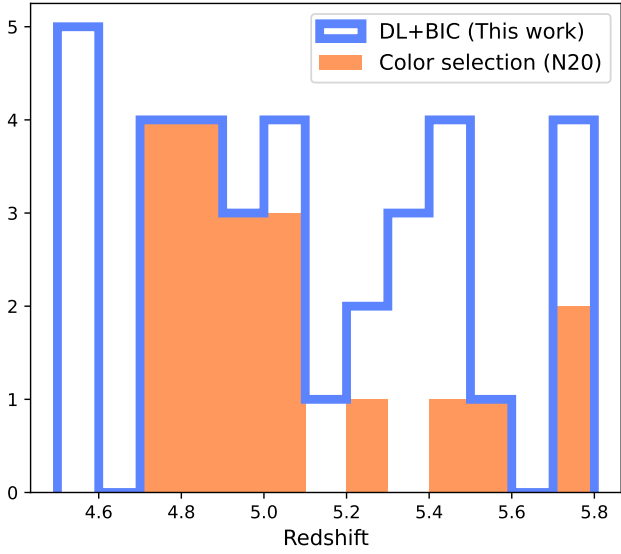
Figure 5. Redshift histograms of the final quasar candidates (blue) and the final quasar candidates satisfying traditional color selection (N20, orange).

Table 3

HSC J233107-001014	
$\mathrm{FWHM_{C\,IV}}\,[\mathrm{km\,s^{-1}}]$	2230^{+1560}_{-640}
$\log(L_{\mathrm{Bol}}\,[\mathrm{erg\,s^{-1}}])$	$45.85^{+0.06}_{-0.05}$
$\log(M_{\mathrm{BH}}\,[M_\odot])$	$7.92^{+0.62}_{-0.27}$
λ_{Edd}	$0.64^{+0.93}_{-0.41}$

uncertainties in the physical parameters caused by the low SNR of the spectra.

Using the bolometric correction derived in (Runnoe et al. 2012), which is

$$\log(L_{\mathrm{Bol}}) = 4.745 + 0.910\log(\,1450\,\text{Å}\,\,L_\lambda(1450\,\text{Å})\,)\,,$$

we calculated the bolometric luminosity of the quasar. For computing the Eddington luminosity L_{Edd}, we use the following equation,

$$\log(L_{\mathrm{Edd}}) = 1.3 \times 10^{38} \times M_{\mathrm{BH}}/M_\odot\ \ \mathrm{erg\,s^{-1}}\,.$$

The Eddington ratio is $L_{\mathrm{Bol}}/L_{\mathrm{Edd}} = 0.64^{+0.93}_{-0.41}$. Table 3 provides the properties of HSC J233107-001014 derived from the line fitting. Figure 4 compares Eddington ratios of quasars at different redshifts in a M_{BH} versus L_{Bol} plane. Compared to quasars at similar luminosities ($L_{\mathrm{Bol}} \sim 10^{46}$ erg s^{-1}; Shen et al. 2011; Trakhtenbrot et al. 2011; Ikeda et al. 2017), this quasar has somewhat a large λ_{Edd} if not exceptional. On the other hand, this λ_{Edd} is on par with brighter quasars at $z \sim 5$ (e.g., Trakhtenbrot et al. 2011; Ikeda et al. 2017; Jeon et al. 2017). This implies that not every faint quasar has smaller λ_{Edd} compared to the bright one. However,

more faint quasars with well-measured BH properties should be required to better understand the accretion activities of $z \sim 5$ quasars.

5. IMPLICATIONS ON QUASAR SELECTION

The confirmation of 4 new quasars brings the total number of spectroscopically confirmed quasars to 9 among 35 candidates. None of the candidates have been shown to be non-quasars so far, suggesting a very high confirmation rate. In addition, there is one quasar candidate with medium-band data, which can be almost certain to be a quasar (Shin et al. 2020).

To quantitatively evaluate the effectiveness of our selection, we compare it to the traditional color selection of N20. We checked whether the 35 final candidates can be selected by N20 selection. It misses 16/35 ($\sim$46%) of the final candidates. Figure 5 shows redshift histograms of the final candidates and the final candidates that meet N20 selection. Since the N20 selection has a high completeness value only when searching for quasars at $4.7 < z < 5.1$, it is difficult to select quasars at $z < 4.7$ or $z > 5.1$. However, our selection method can find quasar candidates at a broader redshift range than the N20 selection does, allowing us to increase the number of quasar sample at $z \sim 5$.

We also calculate the recovery rate of known quasars at $4.5 < z < 5.5$. Our selection process recovers 5/6 known quasars and 4/4 newly discovered quasars (= 9/10, $\sim$90%). We find that one quasar that has been missed is in the parameter space where the completeness is low (see Shin et al. 2022), suggesting that our quasar recovery rate is as high as expected. To firmly confirm the effectiveness of our selection, spectroscopic observations for the 26 remaining candidates is required.

6. SUMMARY

We performed spectroscopic observations for four candidates with $M_{1450} \gtrsim -25.0$ mag at $z \sim 5$ utilizing the DBSP on the 200-inch Hale Telescope in the Palomar observatory. The candidates were selected by deep learning and Bayesian information criterion (Shin et al. 2022). Each candidate has a strong Lyα emission line and clear break near the line in its spectrum, suggesting all the candidates are quasars at $z \sim 5$. 4/4 spectroscopic confirmation rate implies the validity of our novel selection approach. Our selection method provides a possible way for efficiently selecting high-redshift quasars at unbiased redshift ranges from future surveys.

Since HSC J233107-001014 has a strong C IV emission line as well among the quasars, we calculated the marginal BH mass for the quasar, resulting in $10^8\ M_\odot$. The λ_{Edd} of the quasar is $\sim$0.6, although most quasars with a similar luminosity ($L_{\mathrm{Bol}} \sim 10^{46}$ erg s^{-1}) to the quasar have lower Eddington ratios. To better understand the early growth of SMBHs, more faint quasars with $L_{\mathrm{Bol}} \lesssim 10^{46}$ erg s^{-1} should be investigated.

References

Aihara, H., AlSayyad, Y., Ando, M., et al. 2019, Second data release of the Hyper Suprime-Cam Subaru Strategic Program, PASJ, 71, 114

Akiyama, M., He, W., Ikeda, H., et al. 2018, The quasar luminosity function at redshift 4 with the Hyper Suprime-Cam Wide Survey, PASJ, 70, S34

Allard, F., Homeier, D., Freytag, B., et al. 2013, Progress in modeling very low mass stars, brown dwarfs, and planetary mass objects, Memorie della Societa Astronomica Italiana Supplementi, 24, 128

Bañados, E., Venemans, B. P., Mazzucchelli, C., et al. 2018, An 800-million-solar-mass black hole in a significantly neutral Universe at a redshift of 7.5, Nature, 553, 473

Chaves-Montero, J., Bonoli, S., Salvato, M., et al. 2017, ELDAR, a new method to identify AGN in multi-filter surveys: the ALHAMBRA test case, MNRAS, 472, 2085

Coatman, L., Hewett, P. C., Banerji, M., et al. 2017, Correcting C IV-based virial black hole masses, MNRAS, 465, 2120

Coupon, J., Czakon, N., Bosch, J., et al. 2018, The bright-star masks for the HSC-SSP survey, PASJ, 70, S7

Dark Energy Survey Collaboration, Abbott, T., Abdalla, F. B., et al. 2016, The Dark Energy Survey: more than dark energy — an overview, MNRAS, 460, 1270

De Rosa, G., Decarli, R., Walter, F., et al. 2011, Evidence for Non-evolving Fe II/Mg II Ratios in Rapidly Accreting $z \sim 6$ QSOs, ApJ, 739, 56

Fan, X., Strauss, M. A., Richards, G. T., et al. 2006, Constraining the Evolution of the Ionizing Background and the Epoch of Reionization with $z \sim 6$ Quasars. II. A Sample of 19 Quasars, AJ, 131, 1203

Foreman-Mackey, D., Hogg, D. W., Lang, D., et al. 2013, emcee: The MCMC Hammer, PASP, 125, 306

Greene, J. E., Strader, J., & Ho, L. C. 2020, Intermediate-Mass Black Holes, ARA&A, 58, 257

Gwyn, S. D. J. 2012, The Canada-France-Hawaii Telescope Legacy Survey: Stacked Images and Catalogs, AJ, 143, 38

Hickox, R. C. & Alexander, D. M. 2018, Obscured Active Galactic Nuclei, ARA&A, 56, 625

Ikeda, H., Nagao, T., Matsuoka, K., et al. 2017, An Optically Faint Quasar Survey at $z \sim 5$ in the CFHTLS Wide Field: Estimates of the Black Hole Masses and Eddington Ratios, ApJ, 846, 57

Inoue, A. K., Shimizu, I., Iwata, I., et al. 2014, An updated analytic model for attenuation by the intergalactic medium, MNRAS, 442, 1805

Jeon, Y., Im, M., Kim, D., et al. 2017, The Infrared Medium-deep Survey. III. Survey of Luminous Quasars at $4.7 \leq z \leq 5.4$, ApJS, 231, 16

Jiang, L., Fan, X., Vestergaard, M., et al. 2007, Gemini Near-Infrared Spectroscopy of Luminous $z \sim 6$ Quasars: Chemical Abundances, Black Hole Masses, and Mg II Absorption, AJ, 134, 1150

Jiang, L., McGreer, I. D., Fan, X., et al. 2016, The Final SDSS High-redshift Quasar Sample of 52 Quasars at $z > 5.7$, ApJ, 833, 222

Jun, H. D., Im, M., Lee, H. M., et al. 2015, Rest-frame Optical Spectra and Black Hole Masses of $3 < z < 6$ Quasars, ApJ, 806, 109

Kaiser, N., Burgett, W., Chambers, K., et al. 2010, The Pan-STARRS wide-field optical/NIR imaging survey, Proc. SPIE, 7733, 77330E

Kim, Y., Im, M., Jeon, Y., et al. 2018, The Infrared Medium-deep Survey. IV. The Low Eddington Ratio of A Faint Quasar at $z \sim 6$: Not Every Supermassive Black Hole is Growing Fast in the Early Universe, ApJ, 855, 138

Kim, Y., Im, M., Jeon, Y., et al. 2019, The Infrared Medium-deep Survey. VI. Discovery of Faint Quasars at $z \sim 5$ with a Medium-band-based Approach, ApJ, 870, 86

Kim, Y., Im, M., Jeon, Y., et al. 2020, The Infrared Medium-deep Survey. VIII. Quasar Luminosity Function at $z \sim 5$, ApJ, 904, 111

Leauthaud, A., Massey, R., Kneib, J.-P., et al. 2007, Weak Gravitational Lensing with COSMOS: Galaxy Selection and Shape Measurements, ApJS, 172, 219

Liddle, A. R. 2007, Information criteria for astrophysical model selection, MNRAS, 377, L74

Lusso, E., Worseck, G., Hennawi, J. F., et al. 2015, The first ultraviolet quasar-stacked spectrum at $z \simeq 2.4$ from WFC3, MNRAS, 449, 4204

Matsuoka, Y., Iwasawa, K., Onoue, M., et al. 2018, Subaru High-z Exploration of Low-luminosity Quasars (SHELLQs). IV. Discovery of 41 Quasars and Luminous Galaxies at $5.7 \leq z \leq 6.9$, ApJS, 237, 5

Matsuoka, Y., Strauss, M. A., Kashikawa, N., et al. 2018, Subaru High-z Exploration of Low-luminosity Quasars (SHELLQs). V. Quasar Luminosity Function and Contribution to Cosmic Reionization at $z = 6$, ApJ, 869, 150

Matsuoka, Y., Onoue, M., Kashikawa, N., et al. 2019, Discovery of the First Low-luminosity Quasar at $z > 7$, ApJL, 872, L2

Marziani, P., del Olmo, A., Martínez-Carballo, M. A., et al. 2019, Black hole mass estimates in quasars. A comparative analysis of high- and low-ionization lines, A&A, 627, A88

Mazzucchelli, C., Bañados, E., Venemans, B. P., et al. 2017, Physical Properties of 15 Quasars at $z \gtrsim 6.5$, ApJ, 849, 91

McGreer, I. D., Jiang, L., Fan, X., et al. 2013, The $z = 5$ Quasar Luminosity Function from SDSS Stripe 82, ApJ, 768, 105

McGreer, I. D., Fan, X., Jiang, L., et al. 2018, The Faint End of the $z = 5$ Quasar Luminosity Function from the CFHTLS, AJ, 155, 131

Mortlock, D. J., Warren, S. J., Venemans, B. P., et al. 2011, A luminous quasar at a redshift of $z = 7.085$, Nature, 474, 616

Niida, M., Nagao, T., Ikeda, H., et al. 2020, The Faint End of the Quasar Luminosity Function at $z \sim 5$ from the Subaru Hyper Suprime-Cam Survey, ApJ, 904, 89

Oke, J. B. & Gunn, J. E. 1983, Secondary standard stars for absolute spectrophotometry, ApJ, 266, 713

Onoue, M., Kashikawa, N., Matsuoka, Y., et al. 2019, Subaru High-z Exploration of Low-luminosity Quasars (SHELLQs). VI. Black Hole Mass Measurements of Six Quasars at $6.1 \leq z \leq 6.7$, ApJ, 880, 77

Pâris, I., Petitjean, P., Aubourg, É., et al. 2018, The Sloan Digital Sky Survey Quasar Catalog: Fourteenth data release, A&A, 613, A51

Prochaska, J. X., Hennawi, J., Westfall, K., et al. 2020, PypeIt: The Python Spectroscopic Data Reduction Pipeline (v1.3), Zenodo:4323006

Prochaska, J., Hennawi, J., Westfall, K., et al. 2020, PypeIt: The Python Spectroscopic Data Reduction Pipeline, The Journal of Open Source Software, 5, 2308

Reed, S. L., McMahon, R. G., Martini, P., et al. 2017, Eight new luminous $z \geq 6$ quasars discovered via SED model fitting of VISTA, WISE and Dark Energy Survey Year 1 observations, MNRAS, 468, 4702

Runnoe, J. C., Brotherton, M. S., & Shang, Z. 2012, Updating quasar bolometric luminosity corrections, MNRAS, 422, 478

Schlegel, D. J., Finkbeiner, D. P., & Davis, M. 1998, Maps of Dust Infrared Emission for Use in Estimation of Reddening and Cosmic Microwave Background Radiation Foregrounds, ApJ, 500, 525

Selsing, J., Fynbo, J. P. U., Christensen, L., et al. 2016, An X-Shooter composite of bright $1 < z < 2$ quasars from UV to infrared, A&A, 585, A87

Shin, S., Im, M., Kim, Y., et al. 2020, The Infrared Medium-deep Survey. VII. Faint Quasars at $z \sim 5$ in the ELAIS-N1 Field, ApJ, 893, 45

Shin, S., Im, M., & Kim, Y. 2022, The quasar luminosity function at $z \sim 5$ via deep learning and Bayesian information criterion, ApJ, in press

Shen, Y., Richards, G. T., Strauss, M. A., et al. 2011, A Catalog of Quasar Properties from Sloan Digital Sky Survey Data Release 7, ApJS, 194, 45

Shen, Y., Wu, J., Jiang, L., et al. 2019, Gemini GNIRS Near-infrared Spectroscopy of 50 Quasars at $z \gtrsim 5.7$, ApJ, 873, 35

Sulentic, J. W., del Olmo, A., Marziani, P., et al. 2017, What does C IV $\lambda 1549$ tell us about the physical driver of the Eigenvector quasar sequence?, A&A, 608, A122

Trakhtenbrot, B., Netzer, H., Lira, P., et al. 2011, Black Hole Mass and Growth Rate at $z \simeq 4.8$: A Short Episode of Fast Growth Followed by Short Duty Cycle Activity, ApJ, 730, 7

Trakhtenbrot, B., Volonteri, M., & Natarajan, P. 2017, On the Accretion Rates and Radiative Efficiencies of the Highest-redshift Quasars, ApJL, 836, L1

Vestergaard, M. & Peterson, B. M. 2006, Determining Central Black Hole Masses in Distant Active Galaxies and Quasars. II. Improved Optical and UV Scaling Relationships, ApJ, 641, 689

Wang, F., Yang, J., Fan, X., et al. 2021, A Luminous Quasar at Redshift 7.642, ApJL, 907, L1

Willott, C. J., Albert, L., Arzoumanian, D., et al. 2010, Eddington-limited Accretion and the Black Hole Mass Function at Redshift 6, AJ, 140, 546

Woo, J.-H., Schulze, A., Park, D., et al. 2013, Do Quiescent and Active Galaxies Have Different M_{BH}-σ_* Relations?, ApJ, 772, 49

Yang, J., Wang, F., Fan, X., et al. 2020, Pōniuā'ena: A Luminous $z = 7.5$ Quasar Hosting a 1.5 Billion Solar Mass Black Hole, ApJL, 897, L14

Yang, J., Wang, F., Fan, X., et al. 2020, Measurements of the $z \sim 6$ Intergalactic Medium Optical Depth and Transmission Spikes Using a New $z > 6.3$ Quasar Sample, ApJ, 904, 26

Zuo, W., Wu, X.-B., Fan, X., et al. 2020, C IV Emission-line Properties and Uncertainties in Black Hole Mass Estimates of $z \sim 3.5$ Quasars, ApJ, 896, 40